Bulletin of the Seismological Society of America, Vol. 70, No. 5, pp. 1699–1714, October 1980

MODELING THE LONG-PERIOD BODY WAVES FROM SHALLOW EARTHQUAKES AT REGIONAL RANGES

By D. V. Helmberger and G. R. Engen

ABSTRACT

A procedure for modeling *P* and *PL* waves recorded on long-period WWSSN instruments at ranges 1° to 12° is presented. Following the experience gained by modeling explosions (Helmberger, 1972), we demonstrate that these long-period phases are adequately treated by a single crustal layer for most of Western United States. After generating the Green's functions at the various ranges for the three fundamental dislocation types, we need only construct linear combinations of these vectors to represent any arbitrary oriented earthquake. The waveform patterns produced from the various fault types are quite diagnostic with the dip-slip orientations showing a strong ringing nature which is caused by the vertical *SV* lobes. To test the usefulness of this technique, we construct synthetics for some well-studied west coast earthquakes where the orientation, time history, and moment have been determined independently. Comparing the predicted seismograms with observations, we find good agreement in waveshapes and amplitudes.

Introduction

In recent years, our understanding of earth structure and of earthquakes has increased substantially because of our increased ability to interpret seismograms. Much of this progress can be directly attributed to the development of fast techniques for constructing synthetic seismograms where source effects and propagational distortions are treated as separate effects. Following the procedures outlined in Fukao (1971) and Langston and Helmberger (1975), we are able to model the body phases from shallow earthquake sources as distributed shear dislocations with considerable success at teleseismic ranges where the reflected phases from the surface, *pP*, *sP*, etc., are used to great advantage. Unfortunately, only magnitudes between 6 and 7 are sufficiently large to be well recorded by the WWSSN global network at ranges greater than 30°. Once the source parameters are obtained by modeling the teleseismic results, we can treat the source as known and use the observations from 15° to 30° to study the upper-mantle structure, e.g., see Burdick and Helmberger (1978). Unfortunately, these size earthquakes produce *SH* waves that are off-scale at triplication distances. Thus, one must use magnitudes between 5 and 6 to study upper-mantle shear structure with only rough estimates of the source parameters (see Helmberger and Engen, 1974). Secondly, these smaller events are far more abundant geographically and of much importance tectonically. In this paper, we present a technique for using a combination of P_n and *PL* phases recorded at regional distances in the determination of source parameters for these moderate size events.

One of these smaller earthquakes, Truckee, $m = 5\frac{3}{4}$, has been studied by numerous authors. From first-motion studies, it was determined to be a strike-slip event, striking N44°E and dipping 80°SE (Tsai and Aki, 1970). They found the moments of 1.0 and 0.83×10^{25} dyne-cm, respectively, from the Love and Rayleigh wave data. This event was also used by Burdick (1977) to study the upper mantle and, consequently, modeled at teleseismic distances. He used a triangular shape with $\delta t_1 = 1$ and $\delta t_2 = 2$ sec and a moment of 0.6×10^{25} dyne-cm to model the short- and

long-period waveforms. Unfortunately, only a few long-period body waves can be seen beyond 30° so that his moment estimates are weak statistically. On the other hand, the surface waves are clear and on-scale for ranges greater than 10° (see Figure 1). Thus, we will assume Tsai and Aki's (1970) moment estimates and Burdick's time functions and predict the P_n and PL waveshapes and amplitudes at all the stations less than 12° to test the usefulness of our technique.

We will be concerned with the beginning portion of the seismograms, essentially that portion of the record that has apparent velocities greater than the shear waves. At the start of the record, the motions are completely dominated by the P waves (P_n) and moving back into the record, the motion contains progressively more SV contributions (PL). We will call this wave group P_{nl} for brevity which would include the first 2 min of record in Figure 1 as an example.

P_{nl} is polarized mostly in the vertical plane as can be seen in Figure 2 where a

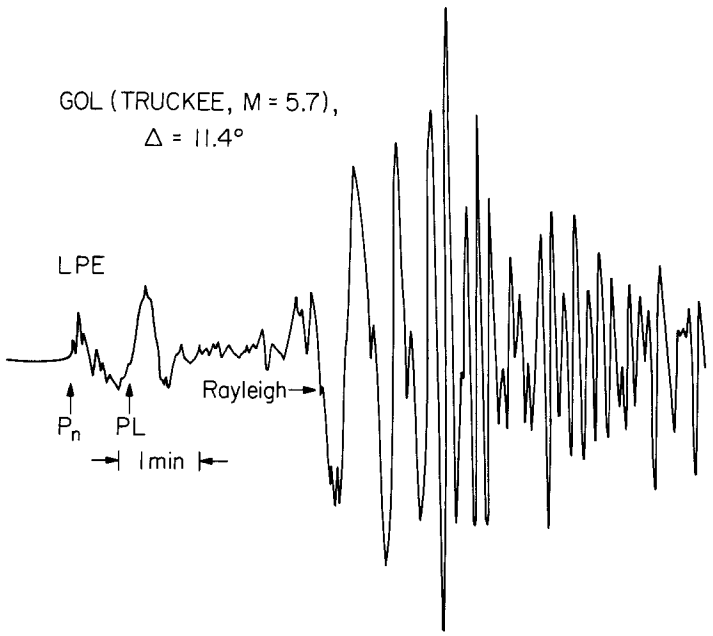

FIG. 1. Observation of the Truckee earthquake (M = 5.7) as recorded on a long-period WWSSN (30, 90) instrument at Golden, Colorado.

naturally rotated motion is recorded. In general, we find that the relative strengths of the NS and EW components can be accurately estimated from the geometry which helped motivate this study. A display of the radial components found by either a summation of the EW and NS motions or by projection are given in Figure 3. Note that the amplitudes at the nodal stations, BOZ and TUC, are relatively small and that the polarities of the P_n's are in agreement with the focal mechanism. We will be primarily interested in modeling the vertical and radial motions at these ranges.

SYNTHETIC P_{nl}

We will assume that earthquakes can be represented by a point shear dislocation and that the earth can be treated by a single layer (crust) over a half-space (mantle); both assumptions are oversimplifications but as we will see, worth consideration as viable models at long periods. The solution in cylindrical coordinates for a point

shear dislocation (double couple) situated in a whole space is discussed at length by Harkrider (1976) and Helmberger and Harkrider (1978). Using generalized ray expansions in conjunction with the Cagniard-deHoop technique, we express the vertical displacement as

$$W(r, o, \theta, t) = \frac{M_0}{4\pi\rho_o}\frac{d}{dt}\left[D(t)^* \sum_{j=1}^{3} A_j W_j\right] \tag{1}$$

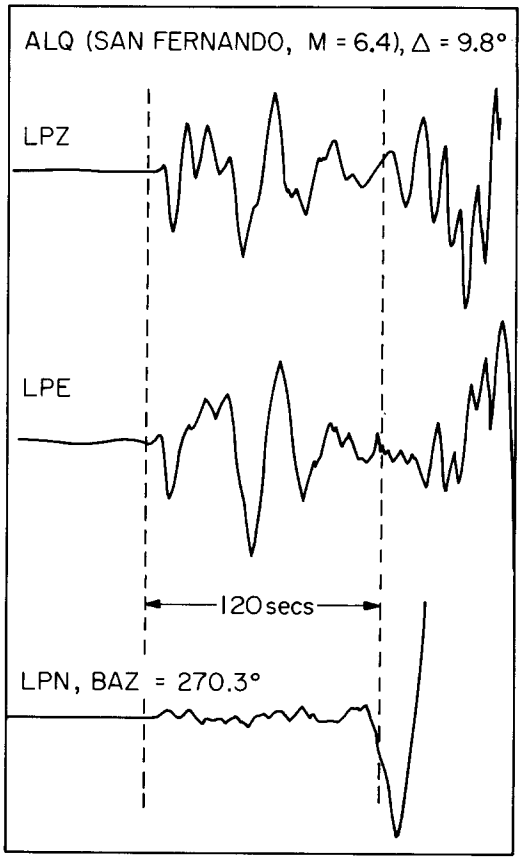

FIG. 2. Three-component observation of the San Fernando earthquake recorded at ALQ, New Mexico, showing the motion to be almost entirely (P, SV) dominated.

where

$$W_j(t) = \sqrt{\frac{2}{r}}\frac{1}{\pi}\left[\frac{1}{\sqrt{t}} * \sum_{i=1}^{n} Im\left(\frac{\sqrt{p}}{\eta_\alpha} C_j(p) R_{NZ}(p) \pi_i(p) \frac{dp}{dt}\right)_i\right]$$

$$+\sqrt{\frac{2}{r}}\frac{1}{\pi}\left[\frac{1}{\sqrt{t}} * \sum_{i=1}^{n} Im\left(\frac{\sqrt{p}}{\eta_\beta} SV_j(p) R_{NZ}(p) \pi_i(p) \frac{dp}{dt}\right)_i\right] \tag{2}$$

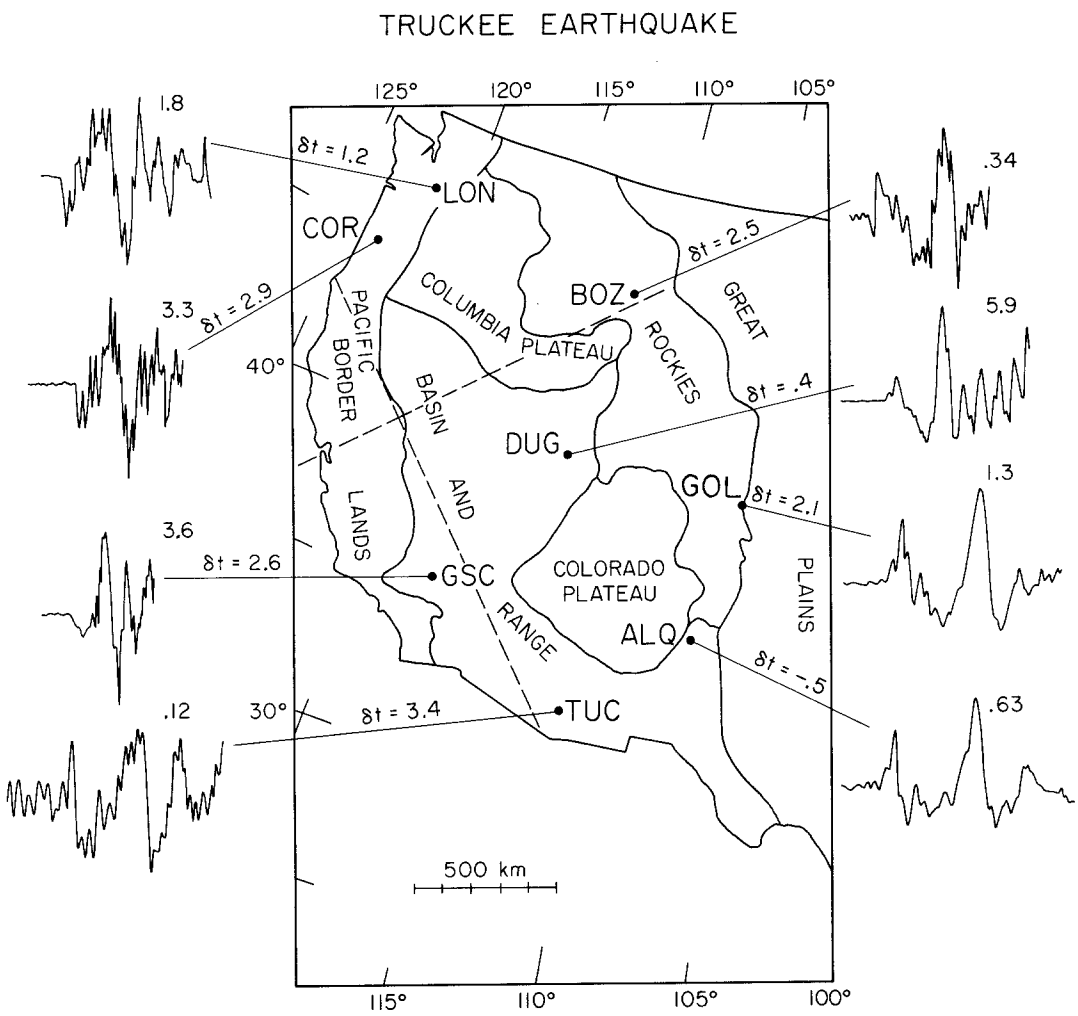

FIG. 3. Map of stations and event (indicated by the crossing fault plane lines). The numbers above the radial observations indicate the amplitudes (cm $\times 10^{-3}$) as measured peak to peak, The δt's are time delays, theoretical minus observed, to be discussed later in the text.

with

p = ray parameter

$$\eta_v = \left(\frac{1}{v^2} - p^2\right)^{1/2}$$

α = compressional velocity

β = shear velocity

ρ = density

M_0 = seismic moment

$\dot{D}(t)$ = far-field time history

and with the orientation constants given by

$$A_1(\theta, \lambda, \delta) = \sin 2\theta \cos \lambda \sin \delta + \frac{1}{2} \cos 2\theta \sin \lambda \sin 2\delta$$

$$A_2(\theta, \lambda, \delta) = \cos \theta \cos \lambda \cos \delta - \sin \theta \sin \lambda \cos 2\delta$$

$$A_3(\theta, \lambda, \delta) = \frac{1}{2} \sin \lambda \sin 2\delta$$

where

θ = strike from the end of the fault plane

λ = rake angle

δ = dip angle.

The vertical radiation patterns patterns are defined by

$$C_1 = -p^2 \qquad SV_1 = -\epsilon p \eta_\beta$$

$$C_2 = 2\epsilon p \eta_\alpha \qquad SV_2 = (\eta_\beta{}^2 - p^2)$$

$$C_3 = (p^2 - 2\eta_\alpha{}^2) \qquad SV_3 = 3\epsilon p \eta_\beta$$

where

$$\epsilon = \begin{matrix} +1 & z > h \\ -1 & z < h. \end{matrix}$$

We are using the same notation and conventions used by Langston and Helmberger (1975). Note that W is positive for downward motions. The summation is over contributing rays where the function $\pi_i(p)$ defines the product of all transmission and reflection coefficients along the path from the source to the receiver. The function $R_{NZ}(p)$ is defined by $R_{PZ}(p)$ or $R_{SZ}(p)$ depending on the mode of propagation upon arrival at the receiver, with

$$R_{PZ} \equiv \frac{2\eta_\alpha(\eta_\beta{}^2 - p^2)}{\beta^2 R(p)}$$

$$R_{SZ} \equiv \frac{\eta_\alpha \eta_\beta}{\beta^2 R(p)}$$

$$R(p) \equiv (\eta_\beta{}^2 - p^2)^2 + 4p^2 \eta_\alpha \eta_\beta.$$

The radial displacements, Q_i, are obtained by replacing R_{PZ} and R_{SZ} by R_{PR} and R_{SR} defined by

$$R_{PR} = \frac{-4\eta_\alpha \eta_\beta p}{\beta^2 R(p)}$$

$$R_{SR} = \frac{2\eta_\beta(\eta_\beta{}^2 - p^2)}{\beta^2 R(p)}.$$

The above high-frequency solution has many advantages in model studies due to its simplicity. However, for small r and long periods, one must use more terms in the expansion or the full solution (see Helmberger and Harkrider, 1978). Since we are primarily interested in regional distances, 100 km $< \Delta <$ 1400 km, we can neglect the near-field effects for the moderate-sized events of interest.

In the remaining portion of this section we discuss the motions produced by the three fundamental faults. Normally, we generate and save the $W_j(t)$ and $Q_j(t)$ specified by expression (2) and construct various solutions for arbitrary (θ, λ, δ) and assumed time history. For presentation, it is convenient to perform the convolution indicated by (1) which more clearly displays the broadband nature of the motions. Thus, we will assume the $\dot{D}(t)$ is specified by a symmetric trapezoidal shape with a 1.5-sec duration which is about the expected period for a moderate-sized event. We will adopt the same units used by Helmberger and Malone (1975), namely if we express r in km, time in sec, ρ_o in gm/cm^3, velocity in km/sec, M_0 in dyne-cm, and displacements in centimeters, we must include a factor of (10^{20}) for unit conversion. In what follows, we assume that $M \times 10^{-20}/4\pi\rho_o = 1$ or $M_0 = 4\pi\rho_o \times 10^{20}$ dyne-cm. The assumed crustal model is given in Table 1.

Constructing the solution by summing the rays as described by equation (2) is tedious in that many rays are required to produce reliable synthetics at the larger ranges. To ensure stability, ray files containing increasing numbers of multiples are computed sequentially where the output is monitored per multiple. An example calculation is displayed in Figure 4 to show the convergence with the addition of

TABLE 1

CRUSTAL MODEL

P_{VEL}	S_{VEL}	Density	Layer Thickness
6.2	3.5	2.7	32.0
8.2	4.5	3.4	

multiples as well as to introduce some geometrical considerations. Since the strengths and polarities of the various rays are strongly influenced by the vertical radiation patterns, $C_j(p)$ and $SV_j(p)$, we have included these patterns above each column. In the strike-slip (SS) case, the direct P and diffracted P along the free surface, included in the direct S generalized ray, are in phase but out of phase in the dip-slip (DS) case. Note that due to our limited time window we do not include the direct S pulse which at this range would be embedded in the Rayleigh wavetrain. The rays appropriate for reflections are leaving the source near the horizontal and because of the position of the P loops produce strong reflections for SS events and weak reflections in the DS case. The opposite is true with respect to the headwaves. The strong downswing in the DS case a few seconds after the onset is produced by the phase *sPP*. Thus, the source depth is a major variable in the DS wavetrain. Note that the beginning portion of P is stable with the addition of multiples but that the later portion, PL part, is more complex requiring large numbers of mixed *P-SV* mode rays for its definition. These synthetics were generated by summing all 4,094 rays as a check against a much smaller ray set which contains kinematic redundancies. For instance only 304 rays were used for the fifth bounce instead of 3,072. Taking advantage of these symmetries allows for relatively inexpensive seismograms, see Hron and Kanasewich (1971).

Another strategy for understanding these motions is to split these ray contributions into those starting upward as opposed to downward at the source as indicated

in Figure 5. The summation process suppresses the short periods in the SS case while emphasizing the long periods. The opposite effect is produced in the DS case. Changing the source depth shifts the upgoing trace relative to the downgoing trace and produces a dramatic effect in the DS case as displayed in Figure 6. In fact, a

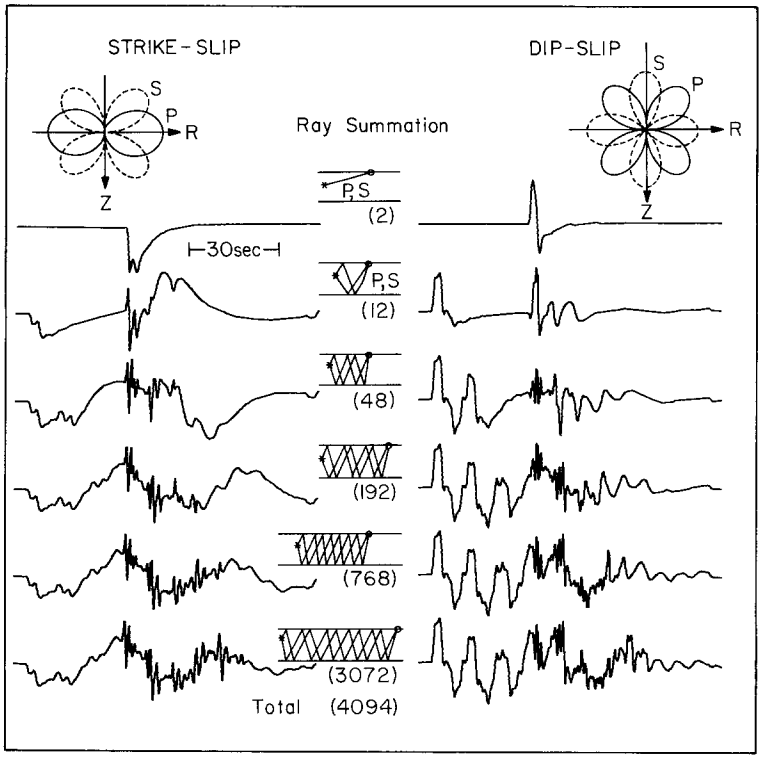

FIG. 4. Vertical components of motion as a function of ray summation assuming a trapezoidal time function described by 0.5, 0.5, 0.5, for pure strike-slip and dip-slip orientations at $\Delta = 1000$ km.

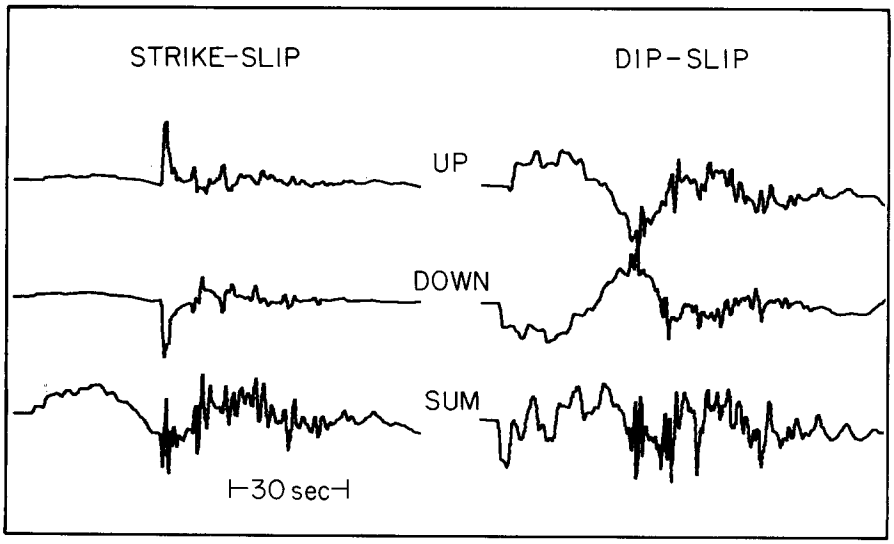

FIG. 5. Radial components of motion at $\Delta = 1000$ km in terms of upgoing, downgoing, and summed for trapezoidal time history (0.5, 0.5, 0.5 sec).

good approximate seismogram for $h = 4$ and 16 can be obtained by simply shifting the $h = 8$ traces without recomputing the rays.

We can also use these split Green's functions to simulate directivity by assuming different source histories for upgoing versus downgoing traces; i.e., perform the convolution given by (1) before summing the traces. This procedure neglects the dependence of directivity on ray parameter which is probably justified because the long-period waveshape is almost entirely controlled by refracted energy which leaves the source with the same ray parameter.

A close examination of Figure 6 reveals that increasing h has the effect of increasing the separation between P_n and direct P or increasing dispersion. A similar effect is produced by increasing the distance as can be seen in Figures 7 to 9 where we display P_{nl} as a function of range.

The broadband displacements given in Figures 7 to 9 suggest that the long-period behavior is independent of the short periods at the larger ranges. Constructing

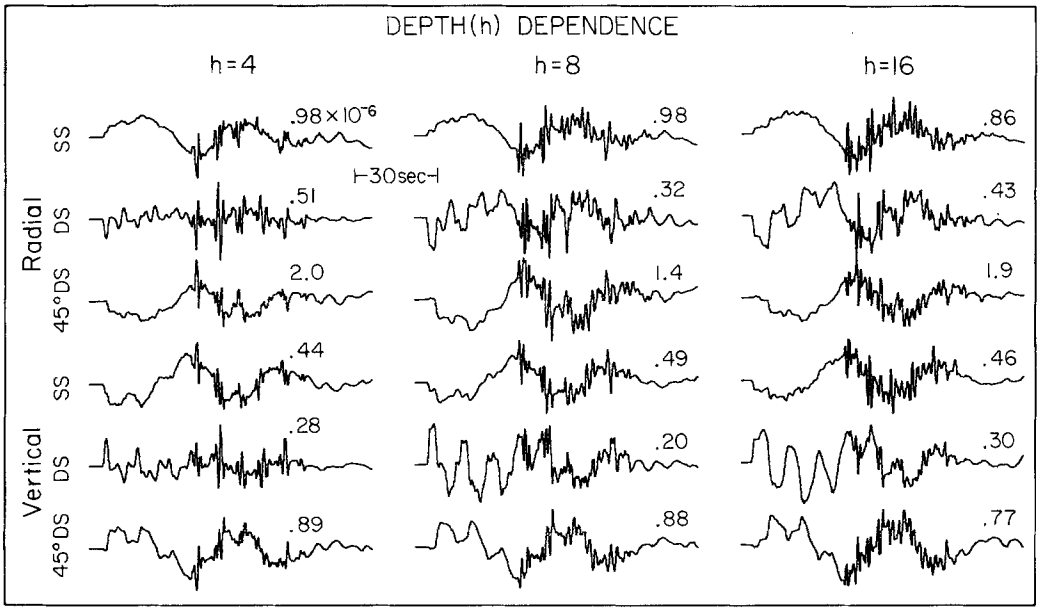

FIG. 6. Motions of all three types of faults at $\Delta = 1000$ km as a function of source depth. The numbers above each trace indicate the zero to peak amplitude in centimeters assuming $M_0 = 4\pi\rho_o \times 10^{20}$ dyne-cm and trapezoidal time history (0.5, 0.5, 0.5 sec).

synthetics appropriate for the WWSSN long- and short-period systems further emphasizes this independence as displayed in Figure 10. Apparently, the long-period synthetics (LP) are dominated by the interference of headwaves while the short-period synthetics (SP) are controlled mostly by interacting moho reflections. Note that the first large pulse on the SP component has an apparent velocity near the compressional velocity of the crustal layer (6.2 km/sec) and combined with its coda contains many of the observed properties of the P_g phase. However, we expect the LP synthetics to be the most useful because of the simplified crustal model assumed in this study.

APPLICATION TO REGIONAL DATA

In this section we will give a brief comparison of some of the regional observations from well-studied earthquakes with theoretical predictions. That is we will suppose

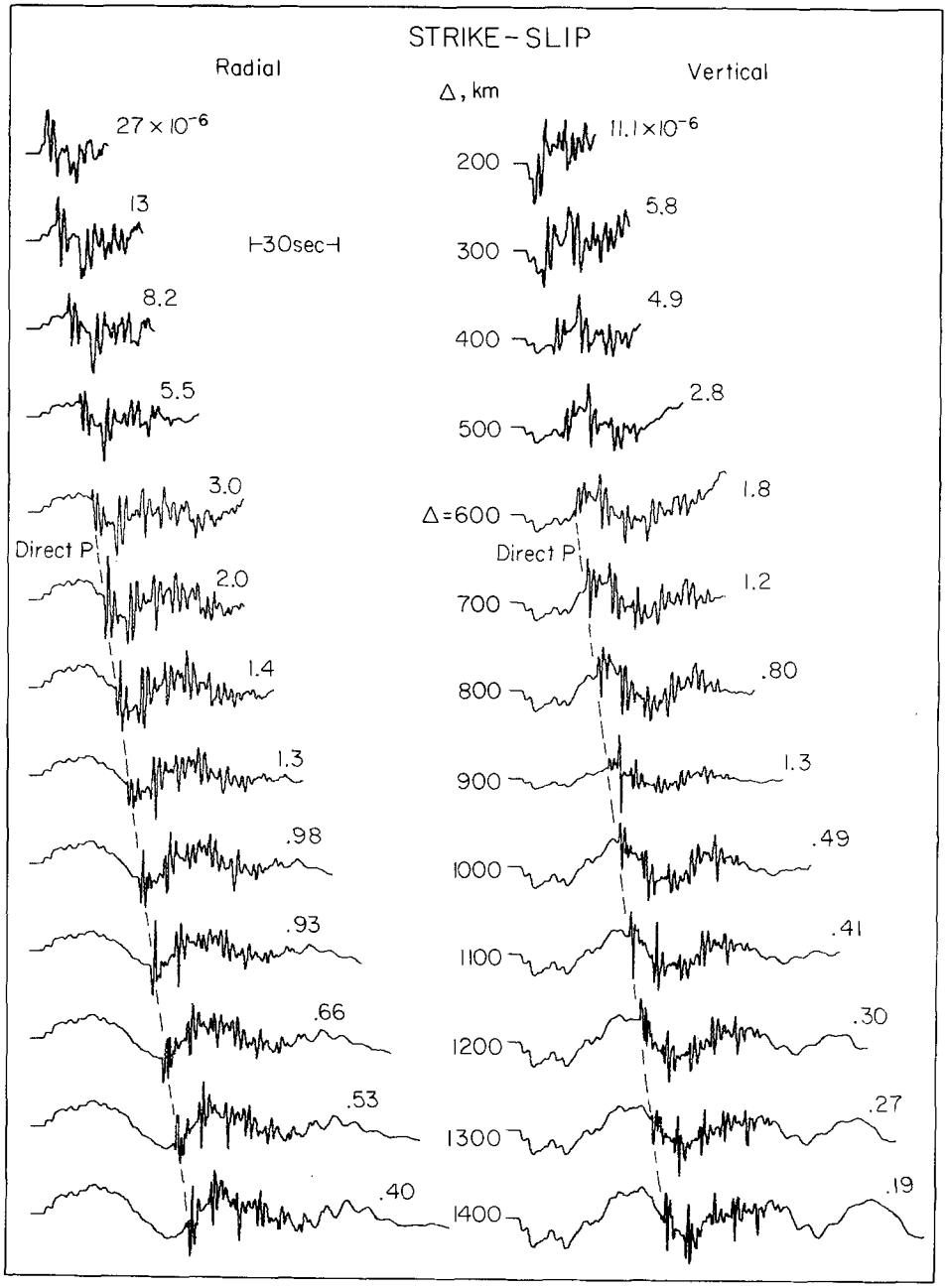

FIG. 7. Strike-slip synthetics as a function of range (Δ) assuming a trapezoidal time history (0.5, 0.5, 0.5 sec) and M_0. The numbers indicate zero to peak amplitudes in centimeters.

that the fault parameters such as fault orientation, moment, and time histories are adequately determined by the surface wave and teleseismic studies and perform the summations indicated by expressions (1) and (2) to generate the synthetic response. We will be primarily concerned with the Truckee earthquake which appears to have produced a fairly complete WWSSN data set as discussed earlier.

Many of the regional P_{nl} phases contain higher frequencies than others, for instance LON and COR of Figure 3 contain considerably more shorter periods than

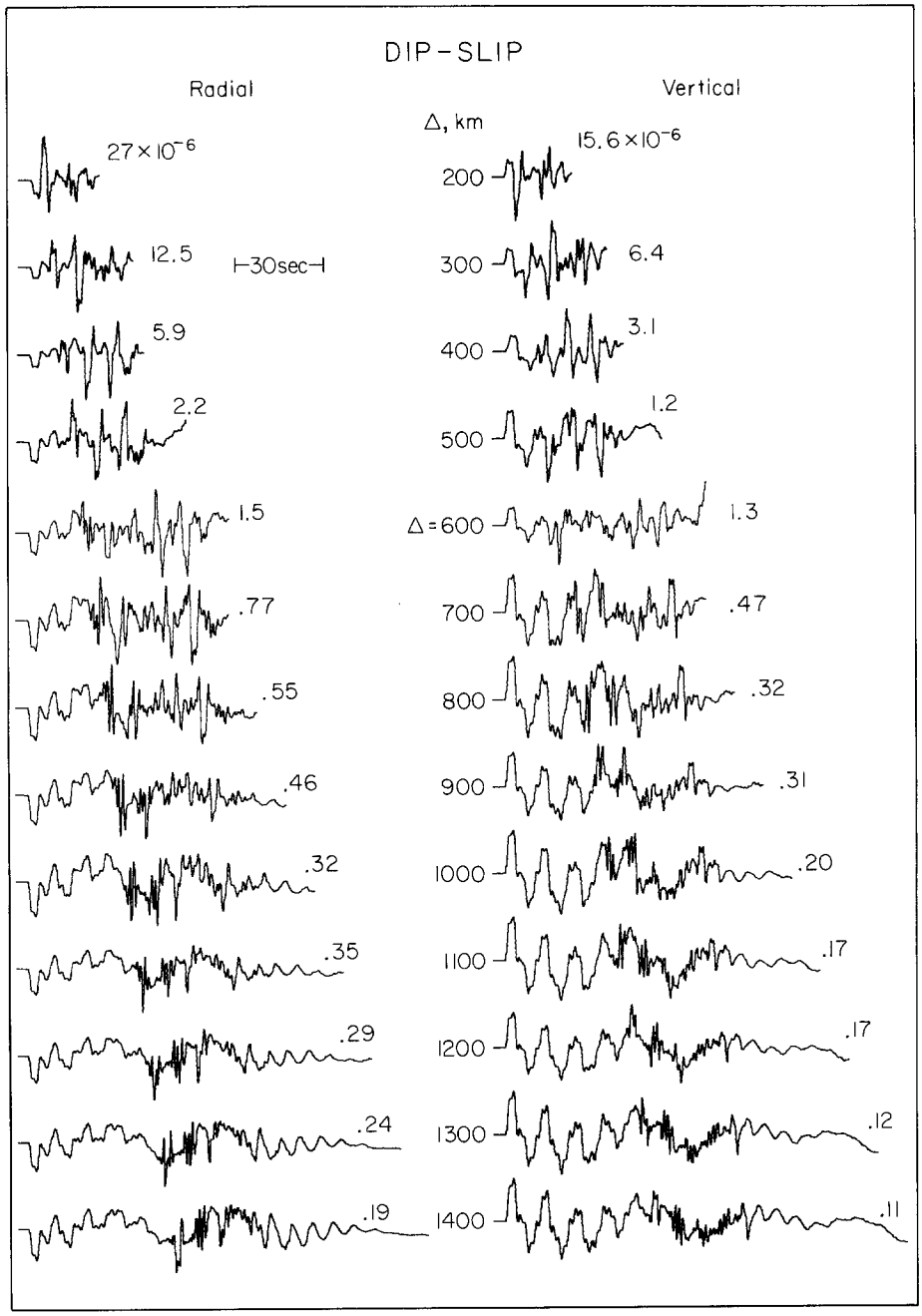

FIG. 8. Dip-slip synthetics as a function of range (Δ) assuming trapezoidal time history (0.5, 0.5, 0.5 sec) and M_0. The numbers indicate zero to peak amplitudes in centimeters.

the southeastern stations. These features could be caused by velocity structure and/or attenuation. A positive gradient below the moho would increase the short-period pulses in the various headwave onsets whereas negative gradient would deplete the shorter periods. Another prominent effect produced by velocity gradients occurs at the free surface where *P*-to-*SV* and *SV*-to-*P* mode conversion plays an important role. Presumably, the shorter wavelengths would experience less mode changes than

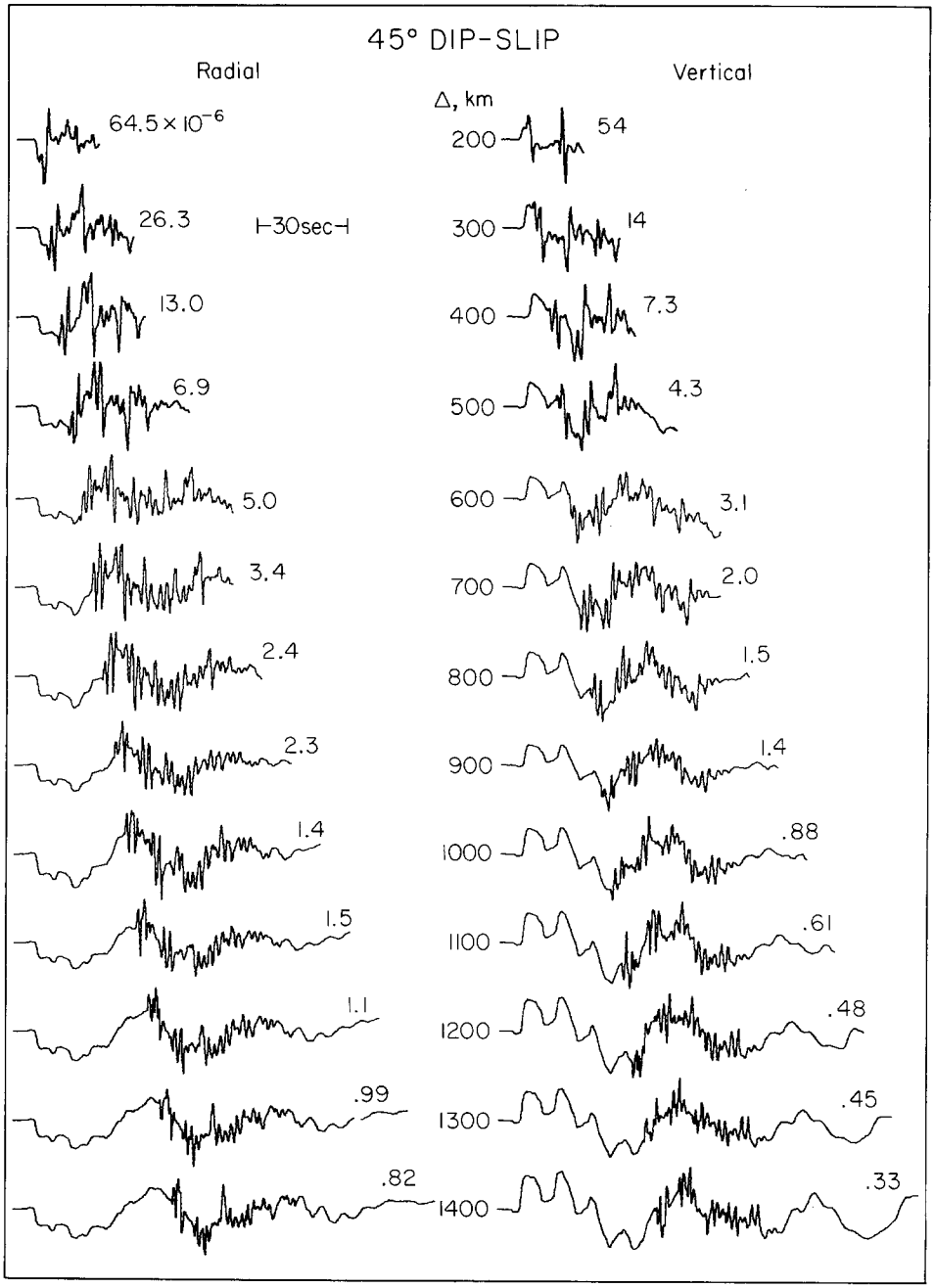

FIG. 9. 45° dip-slip synthetics as a function of range (Δ) assuming trapezoidal time history (0.5, 0.5, 0.5 sec) and M_0. The numbers indicate zero to peak amplitudes in centimeters.

the longer wavelengths and, therefore, one would expect the observed short-period observations to contain more short-period P_n ringing than say the synthetics in Figures 7 to 9. Thus, to help equalize the data set, we have applied a smoothing operator by convolving both data and synthetics with a 2-sec triangle with the results displayed in Figures 11 and 12. This operator has a negligible effect in the synthetics but does remove some of the high frequency from the observed records which can be seen by comparing the waveforms in Figure 3 with Figures 11 and 12.

Note that we did not generate the synthetics at the proper (Δ), but simply used the nearest Green's function in this preliminary analysis. This approximation is probably reasonable at the larger ranges but becomes questionable at the nearer ranges such as GSC. In general, the agreement is surprisingly good except perhaps at the nodal stations where the data are contaminated by noise. Note that the amplitude at TUC is a half-order of magnitude down from ALQ and that the vertical record is mostly a noise sample which has been included here for completeness. The only WWSSN records not shown here are those from BKS which were off-scale.

The predicted waveforms confirm the strike-slip nature of this event. If we scale the amplitude of each synthetic with the corresponding observed record and take the average, we obtain a moment of 0.97×10^{25} ergs which is within 15 per cent of the determination by Tsai and Aki (1970) and well within their error estimate.

Another example of a well-studied strike-slip event is the Borrego Mountain earthquake of 1968 (Allen and Nordquist, 1968). This event produced an excellent

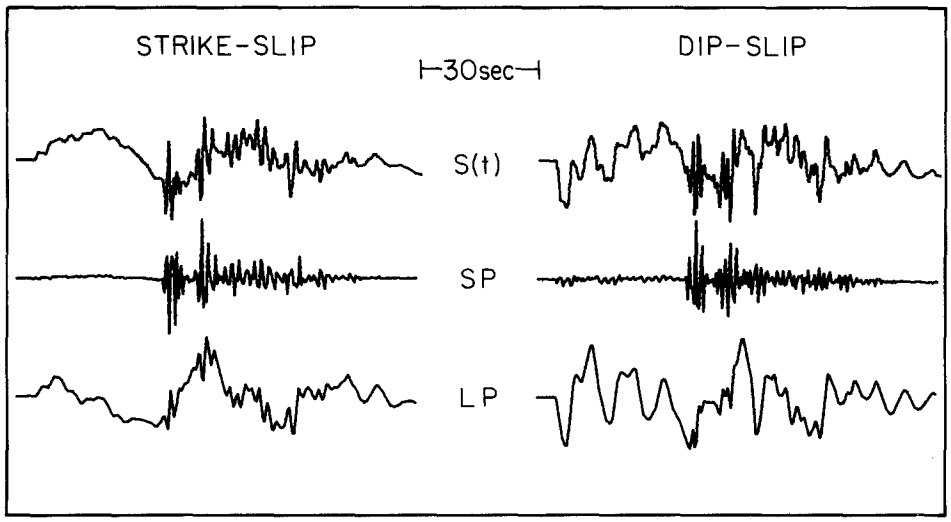

FIG. 10. The *top* traces are the radial displacements at $\Delta = 1000$ km. *Middle* set contains the results after convolving with the WWSSN short-period response and the *bottom* set, the results after applying the long-period response.

set of teleseismic waveforms which have been modeled in great detail by applying a waveform inversion technique (see Burdick and Mellman, 1976). Their results indicate three individual events are involved with the first dominant event having a moment of 1.1×10^{26} ergs and a triangular source history specified by a 0.4-sec rise time followed by a 4.5-sec decay. Because of the large moment, no surface waves were recoverable from WWSSN stations in the United States and only one P_{nl} waveform is completely on-scale. The observations from this station are given in Figure 13 and should be viewed with some caution because of its proximity to a *P-SV* node (6° off) which is the reason for its existence. Nevertheless, the predicted waveform and amplitude is quite good. Adding in the aftershocks proposed by Burdick and Mellman (1976) produced negligible changes in these synthetics.

For our final comparison, we chose the Oroville earthquake which has a normal mechanism ($\theta = 180°$, $\delta = 65°$, $\lambda = -70°$) (see Langston and Butler, 1976). In general, shallow normal events and thrust events are not as well constrained by teleseismic data as strike-slip events. The difficulty arises from the azimuthal

symmetry in the P waveforms where the direct P does not change signs and pP and sP are nearly equal strength and inseparable in time. Thus, the rake angle becomes indeterminant to some degree depending on the quality of the S waveforms. In this situation, the P_{nl} waveforms appear quite useful as displayed in Figure 14 in that a rake near $-90°$ fits the data quite well.

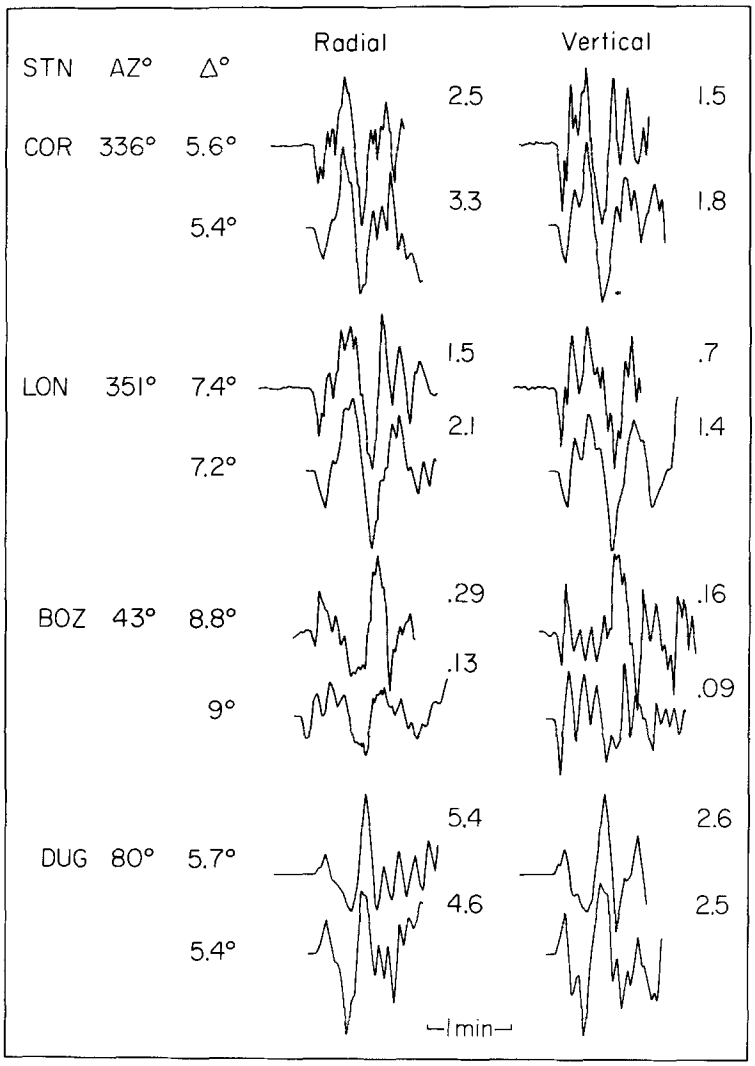

FIG. 11. Comparison of observed waveforms from the Truckee earthquake with synthetic predictions where the numbers above each trace indicate the maximum peak-to-peak amplitude ($\times 10^{-3}$ cm). The assumed source parameters are: $M = 0.83 \times 10^{25}$ ergs, $\theta = 44$, $\delta = 80$, $\lambda = 0$, and triangular time history with $\delta t_1 = 1.0$ and $\delta t_2 = 2.0$. See Figure 3 for station locations.

DISCUSSION

It seems rather surprising that a single layer over a half-space can explain the long-period P_{nl} waveform and amplitude behavior as well as demonstrated in the previous section. However, after conducting a few numerical experiments on more complicated structures, it becomes clear why this simplification works. First, if we examine the behavior of the reflection coefficients R_{pp}, R_{ps}, and R_{sp} for various

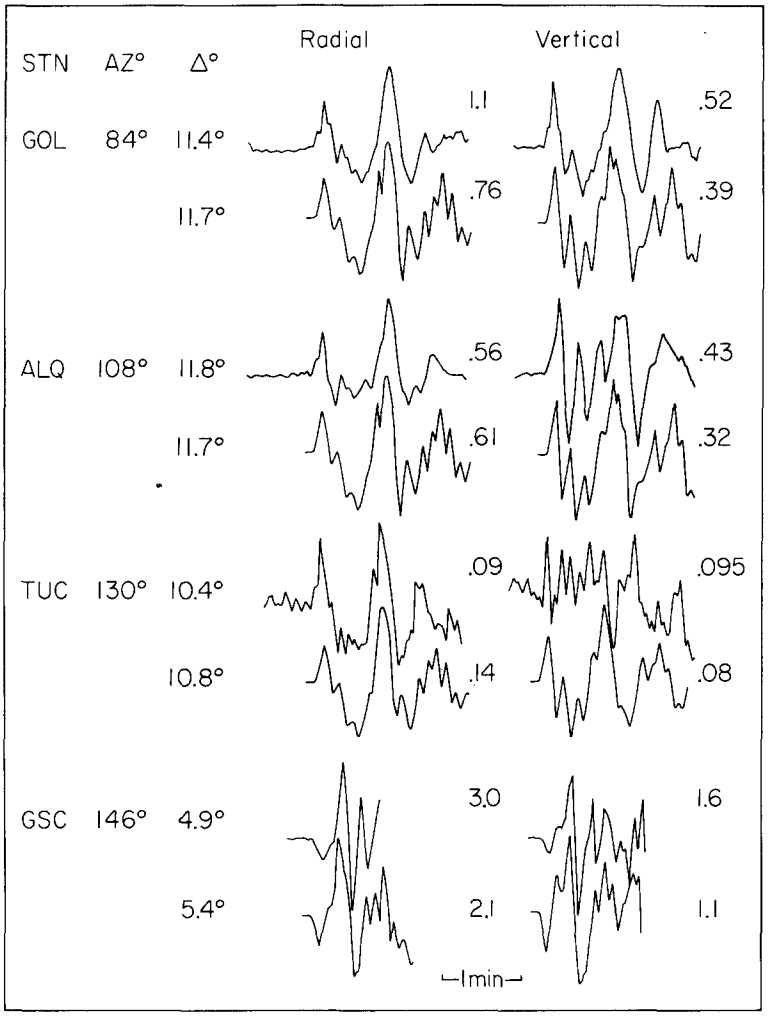

FIG. 12. Continuation of Truckee comparison.

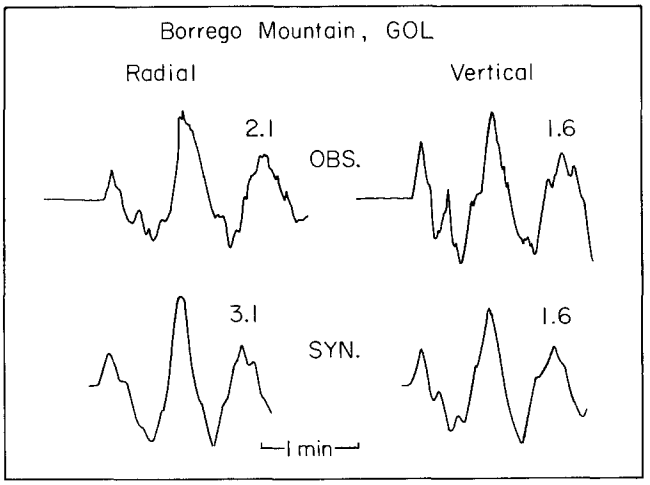

FIG. 13. Comparison of the Borrego Mountain observation obtained at GOL with synthetic prediction where the numbers above each trace indicate the maximum peak-to-peak amplitude ($\times 10^{-3}$ cm). The assumed source parameters are: $M_0 = 1.1 \times 10^{27}$ dyne-cm. $\theta = -45°$, $\delta = 81°$, $\lambda = 178°$, and triangular time history with $\delta t_1 = 0.4$ and $\delta t_2 = 4.5$ sec.

assumptions about the crust-mantle boundary, we find that adding a transition layer of up to 10 km does not drastically alter the long-period behavior at postcritical angles. The numerical experiments presented by Shaw and Orcutt (1979) document this conclusion. At larger ray parameters or apparent crustal velocities, a transition zone has more of an effect especially at small ranges, and this may be the reason for the mismatch at GSC and DUG (see Figures 11 and 12). Another stabilizing feature of P_{nl} is that we expect the multiple reflections to occur either near the source or near the receiver depending on the slopes of the moho. That is, shooting up-dip, crust thinning towards receiver, bunches the reflections near the receiver and shooting down-dip bunches the reflections near the source (see Hong and Helmberger, 1977). Thus variations in the crustal thickness along the path is only sampled by the headwaves which are not likely to be very sensitive. Large crustal changes such as proposed by Eaton (1963) under the Sierra Nevada Mountains may produce significant distortions and should be investigated further both theoretically and observationally.

Variations in crustal thickness and moho velocity does, obviously, alter the absolute P times and relative times between P_n and PL as discussed by Helmberger

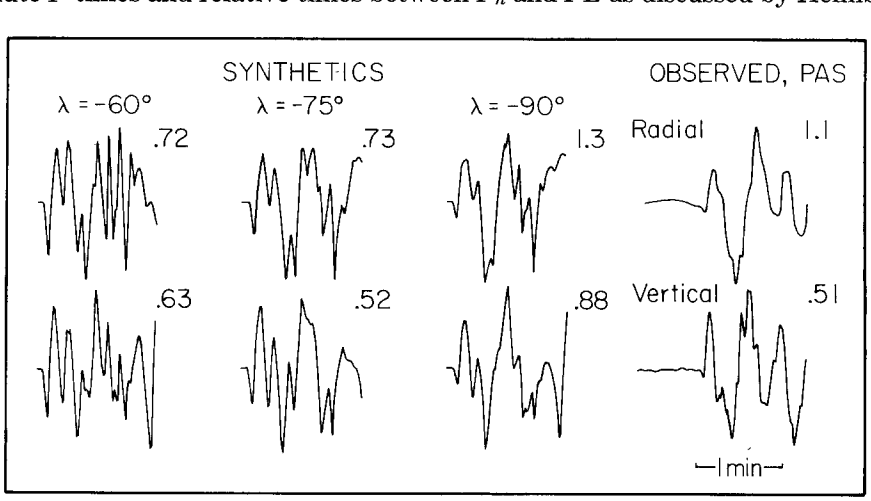

FIG. 14. Comparison of the observed P_{nl} at Pasadena on a long-period (30,100) instrument and synthetics at various rake angles for the Oroville event. The numbers above each trace indicate the peak-to-peak amplitude ($\times 10^{-3}$ cm). The assumed source parameters are: $M_0 = 5.7 \times 10^{24}$ ergs, $\theta = 180°$, $\delta = 65°$, and triangular time history with $\delta t_1 = 1.5$ and $\delta t_2 = 1.5$ sec.

(1973) and York and Helmberger (1973). Note that in the comparisons displayed in Figures 11 and 12, we shifted the theoretical shapes by the (δt's) given in Figure 3. The high P velocity appropriate for the Colorado Plateau causes the negative (δt) or the early arrival time at ALQ relative to TUC. Note that observations to the northwest, namely COR and LON, contain much more short-period energy than do waveforms at other azimuths. One possible explanation is that the upper mantle contains a positive gradient along some azimuths which increases the frequency content of the individual headwaves, e.g., see Hill (1971). On the other hand, the same effect could be caused by differential attentuation along lines or perhaps source directivity. A study of the LRSM and WWSSN array measurements for the many events that crisscross this region could sort out these effects; such a study is in progress.

CONCLUSIONS

We have demonstrated that long-period P_{nl} from earthquakes can be modeled quite successfully by assuming that: (1) the earth is a layer over a half-space; and

(2) earthquakes can be represented by point shear dislocations modeled by three fundamental fault types, strike-slip, dip-slip, and 45° dip-slip. The six components $W_{1,2,3}$ and $Q_{1,2,3}$ defined here can be used directly in inversion schemes of the type discussed by Mellman and Burdick (1976) or they can be used in moment tensor notation as discussed by Stump (1979).

Acknowledgments

This research was supported by the Advanced Research Projects Agency of the Department of Defense and was monitored by the Air Force of Scientific Research under Contract F49620-77-C-0022.

References

Allen, C. R. and J. M. Nordquist (1972). Foreshock, main shock and larger aftershocks of the Borrego Mountain earthquake, *U.S. Geol. Surv. Profess. Paper 787*, 16–23.

Burdick, L. J. (1977). Broad-band seismic studies of body waves, *Ph.D. Thesis*, California Institute of Technology, Pasadena, 68 pp.

Burdick, L. J. and G. R. Mellman (1976). Inversion of the body waves of the Borrego Mountain earthquake to the source mechanism, *Bull. Seism. Soc. Am.* **66,** 1485–1499.

Burdick, L. J. and D. V. Helmberger (1978). The upper mantle P velocity structure of the western United States, *J. Geophys. Res.* **83,** 1699–1712.

Eaton, J. P. (1963). Crustal structure from San Francisco, California, to Eureka, Nevada, from seismic refraction measurements, *J. Geophys. Res.* **68,** 5789–5806.

Fukao, Y. (1971). Seismic body waves from surface faults, *J. Phys. Earth* **19,** 271–281.

Harkrider, D. G. (1976). Potentials and displacements for two theoretical sources, *Geophys. J.* **47,** 97–133.

Helmberger, D. V. (1972). Long-period body-wave propagation from 4° to 13°, *Bull. Seism. Soc. Am.* **62,** 325–342.

Helmberger, D. V. (1973). On the structure of the low-velocity zone, *Geophys. J.* **34,** 251–263.

Helmberger, D. V. and G. R. Engen (1974). Upper mantle shear structure, *J. Geophys. Res.* **79,** 4017–4028.

Helmberger, D. V. and S. D. Malone (1975). Modeling local earthquakes as shear dislocations in a layered halfspace, *J. Geophys. Res.* **80,** 4881–4888.

Helmberger, D. V. and D. G. Harkrider (1978). Modeling earthquakes with generalized ray theory, *Proceedings of IUTAM Symposium: Modern Problems in Elastic Wave Propagation*, J. Miklowitz and J. Achenbach, Editors, John Wiley and Sons, New York.

Hill, D. P. (1971). Velocity gradients and anelasticity from crustal body wave amplitudes, *J. Geophys. Res.* **76,** 3309–3325.

Hong, T. L. and D. V. Helmberger (1977). Generalized ray theory for dipping structure, *Bull. Seism. Soc. Am.* **67,** 995–1008.

Hron, F. and E. R. Kanasewich (1971). Synthetic seismograms for deep seismic sounding studies using asymptotic ray theory, *Bull. Seism. Soc. Am.* **61,** 1169–1200.

Langston, C. A. and D. V. Helmberger (1975). A procedure for modeling shallow dislocation sources, *Geophys. J.* **42,** 117–130.

Langston, C. A. and R. Butler (1976). Focal mechanism of the August 1, 1975 Oroville earthquake, *Bull. Seism. Soc. Am.* **66,** 1111–1120.

Shaw, P. and J. Orcutt (1979). The influence of source parameters and crustal structure on PL propagation, *Trans. Am. Geophys. Union* **60,** 895.

Stump, B. W. (1979). Investigations of seismic sources by the linear inversion of seismograms, *Ph.D. Thesis*, University of California, Berkeley.

Tsai, Y. B. and K. Aki (1970). Source mechanism of the Truckee, California earthquake of September 12, 1966, *Bull. Seism. Soc. Am.* **60,** 1199–1208.

York, J. E. and D. V. Helmberger (1973). Low-velocity zone variations in the southwestern United States, *J. Geophys. Res.* **78,** 1883–1886.

Seismological Laboratory
Division of Geological and Planetary Sciences
California Institute of Technology
Pasadena, California 91125
Contribution No. 3393

Manuscript received February 4, 1980